Eu-doped α-Fe2O3 nanoparticles with modified magnetic properties

(Article begins on next page)

06 June 2024

UNIVERSITÀ DEGLI STUDI DI TORINO

Eu-doped α-Fe2O3 nanoparticles with modified magnetic properties

Abstract

Eu-doping of hematite (α-Fe2O3) nanoparticles (NPs) takes place under hydrothermal conditions, and does not at ambient temperature and pressure. Required circumstances have been studied in detail. In the presence of Eu, besides hematite, some goethite and ferrihydrite are formed. Evidence for the occurrence of doping is reported. Chemical composition, as studied by EDS (bulk) and XPS (surface), reveals an enrichment of Eu at NPs core, ascribed to the occurrence of a two-step mechanism of NP formation, comprising nucleation at first, in which Eu^{3+} ions compete with Fe^{3+} ions, notwithstanding the large difference in concentration, and a successive growth step of NPs in a solution comparatively richer in Fe^{3+} species. The Eu content affects: (i) the morphology of NPs, as shown by TEM and FE-SEM; (ii) lattice parameters, as obtained by Rietveld refinement of XRD patterns; (iii) magnetic properties, due to the presence of Eu^{3+} ions, characterized by a higher one-ion anisotropy and a lower magnetic moment with respect to iron cations.

1. Introduction

Iron oxy-hydroxide and oxide nanoparticles (NPs) with controlled morphology and size have actual and/or potential applications in different fields, such as manufacture of pigments, ceramic materials, gas sensors and magnetic recording [1], [2], [3], [4] and [5]. Magnetic NPs are also becoming more and more interesting for their use in biomedicine, including diagnostic and targeted cancer therapies [4]. Besides their chemical composition, NPs size and morphology may affect their physico-chemical, magnetic properties and their (possible) toxicity, a parameter of paramount importance especially for biological applications [6].

Among iron oxides, hematite (α-Fe2O3) is the most abundant and stable polymorph, end-member of transformations of the other iron oxides. Hematite particles may be obtained at different scales, both nano- and micro-, by different ways, including gas phase methods (CVD, laser pyrolysis, etc.); micro-emulsion (water/oil); transformation of other oxide/hydroxides (e.g. dehydroxlation of goethite); sol–gel synthesis and forced hydrolysis of Fe^{3+} salts [7] and [8]. Such methods yield different products depending on a number of synthesis parameters, which may be properly changed and controlled. For example, some of us recently showed that sub-micrometric hematite particles (larger however than 90 nm) [9] obtained by forced hydrolysis of ferric chloride are characterized by very low or nil toxicity.

Hematite, iso-structural with corundum, can be described by either rhombohedral or hexagonal crystallographic system: Fe3+ cations are octahedrally coordinated to 6 O anions and crystals arise from the repetition of Fe(O)6 octahedra in a relatively open form. As to morphology, different habits may be assumed (hexagonal plate, rhombohedra, spindle, rod, ellipsoid, cube, disc, sphere, star, bipyramid, wire, hollow sphere) [7], as morphology depends, inter alia, on the presence in the synthesis medium of surfactants [10] and [11], cations [3], [12], [13], [14] and [15] and, especially, anions [16], [17], [18] and [19], which all may cause an anisotropic growth by driving it along certain crystallographic directions. For instance, chloride ions (Cl−) restrain the growth in the direction normal to the {0 1 2} faces, so yielding micro particles with a pseudo-cubic shape [18]. On the other hand, both sulphate and phosphate ions perturb the growth along the direction normal to the c-axis, giving ellipsoidal or peanut-type particles, such anionic species being more strongly adsorbed on {1 1 0}, {1 0 0} and {0 1 2} faces [16] and [17].

A way to modify substantially hematite properties, beyond morphology, is the structural incorporation of foreign cations, particularly facile for trivalent cations having similar ionic radius [7]. Guest cations may alter the particles shape, as occurs with Al cations which cause a peanut-like shape [15], or induce change in optical properties, as observed for La-substituted micro-hematite [14]. To this respect, rare-earth elements are an attractive class of dopant elements, as they give easily trivalent cations with peculiar magnetic and optical properties related to their f-electronic configuration. Doping of hematite with rare-earth elements is however challenging, due to the different size of Fe3+ and rare-earth trivalent ions.

The present work reports the synthesis of hematite nanoparticles doped with Eu by forced hydrolysis. The particle morphology has been studied, as well as optical and magnetic properties. The former deserve an ad hoc report, as luminescence properties of Eu complexes are of paramount importance, especially in the solid state [20]. The present work describes instead the changes induced by the presence of Eu in the magnetic properties [7] and [8].

2. Experimental procedure

2.1. Materials synthesis

Precipitation of pure hematite particles from Fe(III) solutions depends on several factors, such as temperature, concentration of ferric cations, type of anions and OH/Fe ratio [7]. The procedure hereafter described is the result of a screening performed in order to optimize the final product. Synthesis was initially carried out at different pH values (1–10) as well as temperatures (353–393 K) of both hydrolysis and aging. With acidic conditions, no inclusions of Eu was evidenced, Eu resulting either as a separated phase or in the supernatant solution, as determined by EDS analysis. Starting from a basic solution and by adjusting to 7.6 the final pH, Eu-containing particles formed only at temperature of aging higher than 353 K: to have a homogeneous distribution of particles, however, aging at 393 K was necessary. Therefore,

the chosen method consisted in the co-precipitation of Eu and iron salts by adding a base in a preheated alkaline solution, followed by one week ageing at 393 K in static and close-to-neutrality conditions.

Two Eu-containing materials with nominal Eu/Fe atomic ratio=2 and 4% (Eu:Hem_2 and Eu:Hem_4, respectively) were prepared as follows: europium(III) chloride (EuCl3·6H2O, 99.99%) was added to a 0.02 M FeCl3·6H2O (ACS reagent) solution. The obtained mixture was drop-wise added to a solution of aqueous ammonia (33 wt%, Riedel-de Häen) and bi-distilled water (Labochem) kept at 368 K: the initially basic pH, dropped to 1.2, was adjusted to 7.6 by adding further aqueous ammonia. The mixture so prepared was poured into a Teflon autoclave, sealed and put in a preheated furnace at 393 K for 7 days. The precipitate was subsequently separated from mother liquid, rinsed several times with bi-distilled water and dried at room temperature. A sample of pure hematite (Hem) was also prepared in the same hydrothermal conditions.

The Eu content of the resulting materials was measured by energy dispersive X-ray spectroscopy (EDS) analysis: results in Table 1 were calculated from five spots with an acquisition time of 50 s each. Other estimates of the composition will be considered below. Because the determination of the amount of oxygen is affected by a large error, being a light atom, data in Table 1 were calculated by setting the sum of the molar fractions of Eu and Fe to 40%, as dictated by stoichiometry.

Table 1.

Chemical composition of the samples (atomic percentage, at%), as obtained by EDS microanalysis.

Element	Sample		
	Hem	Eu:Hem_2	Eu:Hem_4
Eu (at%)	–	2.2	4.1
Fe (at%)	40.6	37.8	35.9

2.2. Methods

XRD measurements were performed on a X'Pert Philips diffractometer (PANalytical B. V.) operating with CuKα radiation (1.541874 Å) in the scan range from 10° to 90° 2θ (step width=0.02° 2θ; time per step 12 s). Phase identification was performed by making reference to the PDF-2 Release 2002 database.

The structural features of the hematite phase were extracted from the powder diffraction patterns by a full-profile refinements with Rietveld method, made by using the GSAS–EXPGUI [21] and [22] package software.

Specific surface area (SSA) was measured according to the BET (Brunauer–Emmett–Teller) method by means of N_2 adsorption at 77 K on powders previously outgassed at 423 K to remove water and other atmospheric contaminants (Quantachrome Autosorb1).

Transmission electron microscopy was used to investigate both particles morphology and chemical composition with a Philips CM12 instrument, operating at 120 kV with a LaB6 filament, coupled with EDS microanalysis probe. Particles size was determined by measuring at least 60 particles on TEM micrographs. Electron diffraction from selected areas (SAED) was performed on the same TEM instrument from several particles to evaluate the degree of crystallinity; simulation of electron diffraction patterns was done by using CaRine Crystallography 3.1 software.

Chemical surface composition was investigated by X-ray photoelectron spectroscopy, (XPS PHI Scanning X-Ray Microprobe AlKα radiation): the C 1s peak at 284.6 eV was used as a reference for charge correction. XPS peaks were curve-fitted by using the MultiPak V6.1A software in the range 536–525 eV with an iterated Shirley background subtraction and Gaussian–Lorentz curve type (90–10%).

Magnetic measurements were performed in the temperature interval 100–320 K on all samples in the form of dry powders, by means of a vibrating sample magnetometer (Lakeshore VSM 7400) operating in the field range −14 kOe<H<14 kOe and equipped with a cryostat. Magnetic hysteresis loops were measured at fixed temperatures from 200 to 320 K. The temperature evolution of remanent magnetization was measured in the interval 100–320 K by continuously varying the sample temperature (always on a cooling ramp in order to avoid thermal hysteresis effects).

3. Results and discussion

3.1. Structural and morphological characterization

Fig. 1 reports XRD patterns of the samples: measured curves (symbols) are superposed to curve-fitted patterns (black lines), along with difference curves (grey lines). Hematite (α-Fe2O3) is the main phase detected with all samples. An additional minor peak (labelled with a letter g) is observed at 2θ=21.24°, corresponding to the most intense peak of goethite (α-FeOOH), the formation of which is expected for

syntheses carried out in highly basic solution [23]. The presence of only one minor peak assignable to goethite does not evidently allow a quantitative estimate of the relative extent of the two phases by means of Rietveld method.
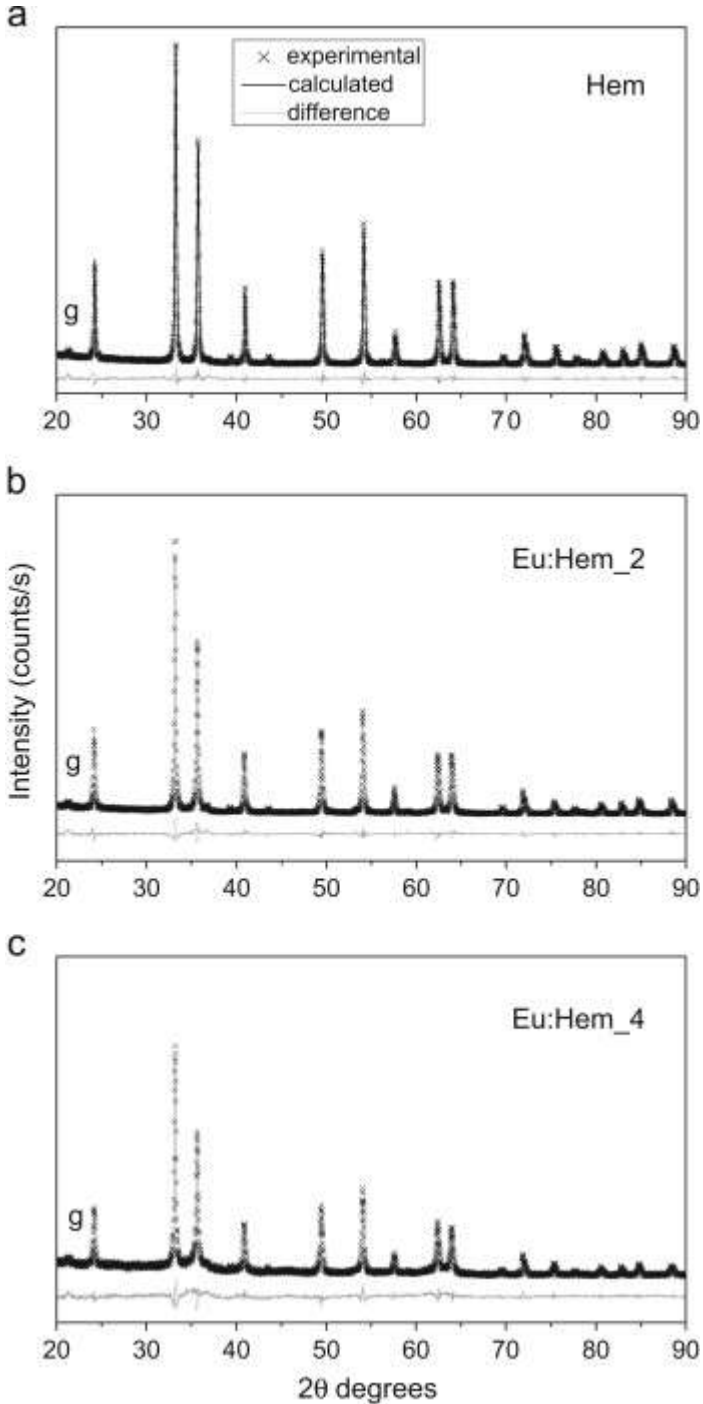

Fig. 1.

XRD patterns, related Rietveld refinements, and corresponding differences concerning: Hem (a); Eu:Hem_2 (b) and Eu:Hem_4 (c). Black symbols: experimental points; black curves: Rietveld refinement results; grey curves: difference between experimental and calculated patterns. The "g" letter stands for goethite (α-FeOOH) main peak.

As better appreciated in Fig. 2a, with Eu:Hem_4 (and to a minor extent also with Eu:Hem_2) two broad signals are observed at ca. 35° and 62° 2θ, where the peaks of 2-line ferrihydrite are expected [24]. The latter is a hydrous ferric oxohydroxide, for which several chemical formulas are proposed with different O/OH ratio, e.g. $Fe_5HO_8·4H_2O$, $Fe_5O_3(OH)_9$ or $5Fe_2O_3·9H_2O$ [3] and [25]. Ferrihydrite is usually the first (poorly crystalline) phase precipitating during hydrolysis of iron salts, especially at neutral-basic pH values [7] and [24] and it is found in two forms, called 2-line or 6-line, respectively, depending on the number of peaks in the XRD pattern [25]. In the present case, therefore, its presence is not surprising, since samples were obtained in alkaline conditions. Moreover, the presence of foreign species (Eu ions, in the present case) within the synthesis medium, besides influencing the kinetics of crystal growth, may also modify the product composition: adsorption of foreign ligands, for instance, usually delays the formation of hematite by the yield of ferrihydrite.
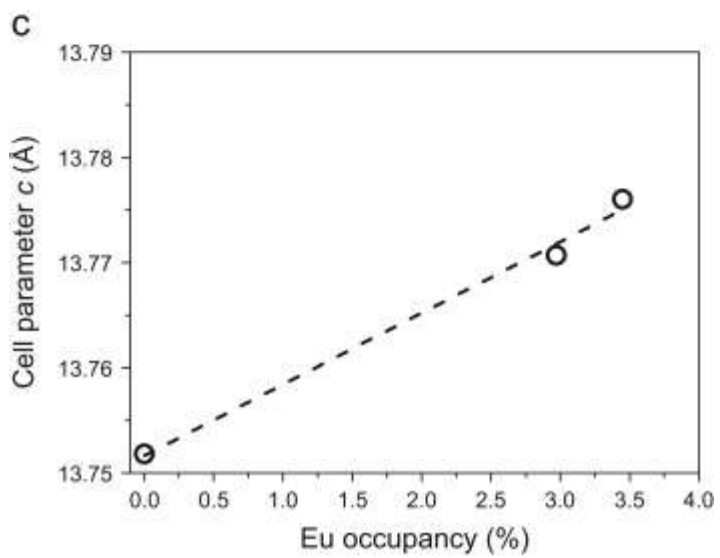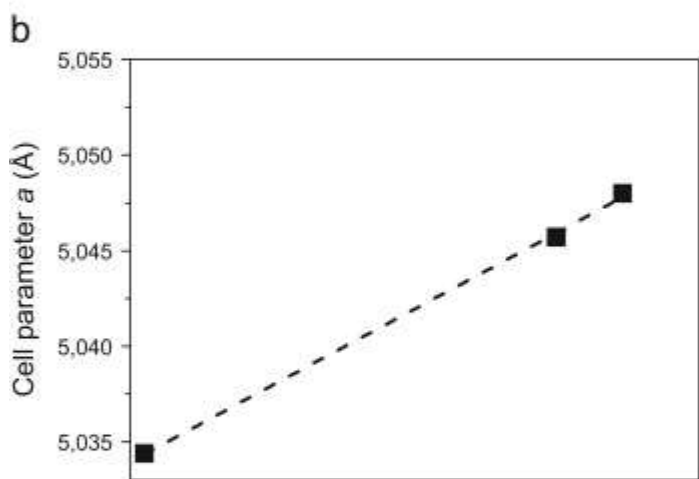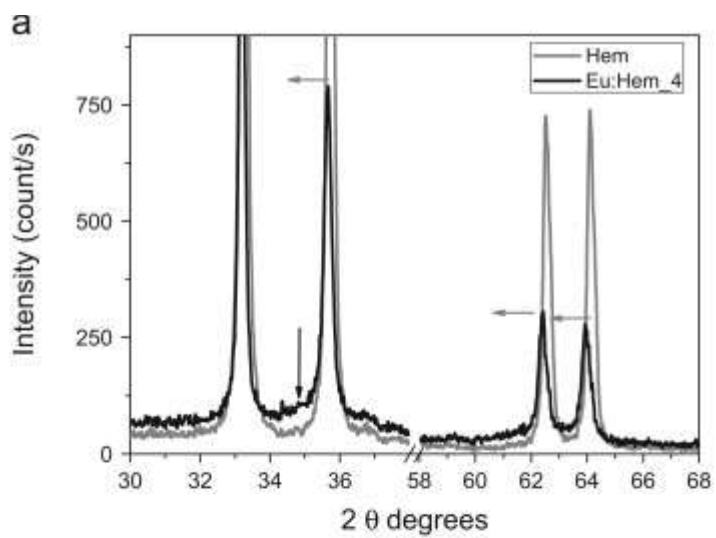
Fig. 2.

Comparison between the XRD patterns of Hem and Eu:Hem_4 in the 30–68° 2θ range (a): downward arrow indicates the signal probably ascribable to 2-line-ferrihydrite in Eu:Hem_4; grey arrows indicate peaks shift towards lower angles in the doped sample. Change in the lattice parameters a (full squares, section (b)) and c (hollow circles, section (c)) as a function of Eu occupancy as calculated by Rietveld method.

Rietveld structural refinements allowed determining Eu occupancy at cation sites and cell parameters in the hematite structure. Results in Table 2 shows that Eu occupancy data are grossly consistent with the nominal amount of Eu added during the synthesis. Discrepancies are instead observed with EDS data, which, however, refer to the whole sample, and not to hematite alone. We will therefore hereafter adopt occupancy data to describe the Eu content of the hematite phases.

Table 2.

Data derived from XRD patterns through Rietveld refinement. Standard deviations in brackets as uncertainties in the last digit.

Sample	Cell edge and cell volume			Eu occupancy (%)	Octahedral distortion (%)	R_{wp}
	a (Å)	c (Å)	Cell volume (Å³)			
Hem	5.0344 (1)	13.7518 (4)	301.85 (1)	–	9.6	0.1247
Eu:Hem_2	5.0457 (1)	13.7707 (5)	303.63 (2)	2.97	9.8	0.1294
Eu:Hem_4	5.0480 (2)	13.776 (1)	304.03 (4)	3.45	10.7	0.1563

Fig. 2a compares the XRD patterns of Hem and Eu:Hem_4 samples in the 30–68° 2θ range: besides the features described above, i.e. the presence of signals attributable to 2-ferrihydrite (downward arrow) in the Eu containing materials, a shift towards lower angles is seen for Eu:He_4 peaks, due to a change in hematite cell parameters. The latter (both a and c) are reported as function of Eu occupancy in Fig. 2b and c, respectively: although only three points are available, a linear trend is observed for both a and c parameters, as expected on the basis of Vegard's law.

An outcome of Rietveld refinement is the measure of the distortion of Fe(O)6 octahedra reported in Table 2. This result also agrees with expectation, because ferric cations in six fold coordination and high spin state have an ionic radius of 0.645 Å, whereas that of Eu3+ is 0.947 Å [26].

Definite changes are observed in NPs morphology. Fig. 3 shows selected TEM micrographs, from which NPs size reported in Table 3 were measured: Hem sample (Fig. 3a) shows mostly hexagonal NPs, having two edges less developed, so that the particles look as squares, with an average size of about 75 nm (±14). Both Eu:Hem_2 and Eu:Hem_ 4 show rice-like particles (Fig. 3b and c, respectively), with one or sometimes both particle extremities forming a sharp angle, δ, of 78° (Eu:Hem_2) and 63° (Eu:Hem_4). Fig. 3d reports a higher magnification TEM picture of Eu:Hem_2 sample, in which ferrihydrite spherical NPs are observed, along with one needle-like particle, ascribed to goethite, in agreement with XRD patterns above. The increase in BET SSA values (Table 3) is probably related to the presence of such small spherical NPs of ferrihydrite, which, having an average dimension of few nanometers, brings about an increase of the measure specific surface area.
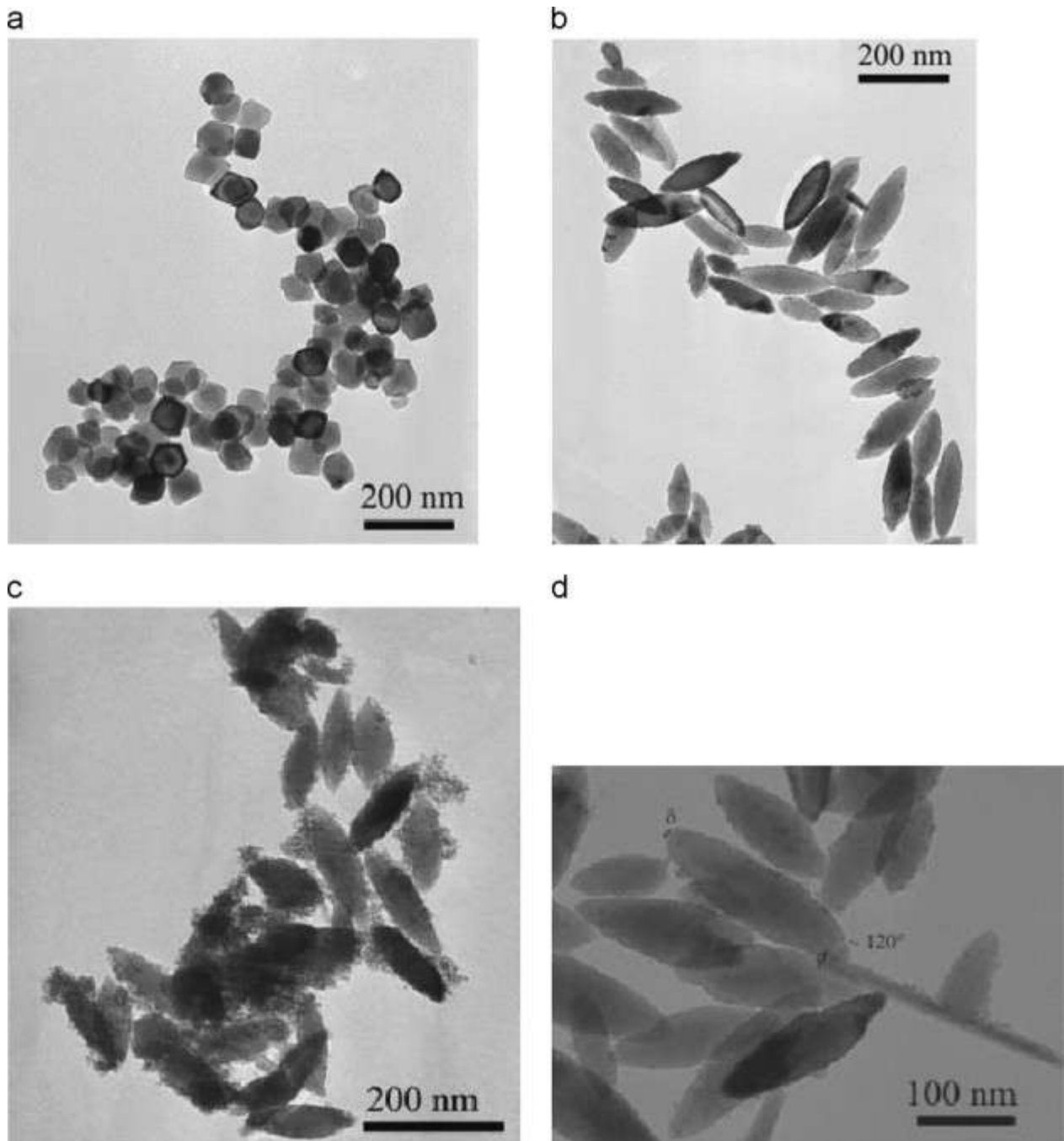
Fig. 3.

Selected TEM micrographs of samples: Hem (a); Eu:Hem_2 (b); Eu:Hem_4 (c). Section (d) reports a micrograph of Eu:Hem_2 taken at a higher magnification, showing ferryhydrite nanoparticles and a goethite needle.

Table 3.

Particle size (nm, standard deviations in brackets), aspect ratio, as measured from TEM micrographs. BET SSA values, as measured by N2 isotherms at 77 K.

Sample	Particle size		Aspect ratio	BET specific surface area ($m^2\,g^{-1}$)
	L_{max}	L_{min}		
Hem	75 (14)	–		21
Eu:Hem_2	159 (48)	58 (11)	2.7	26
Eu:Hem_4	135 (35)	47 (9)	2.9	84

According to the literature, different factors may affect nanoparticles morphology, including pH, but in the present case, changes in NPs morphology are to be attributed to Eu incorporation, probably promoting the crystal growth along a preferential direction, since comparison with Hem NPs, obtained in the same synthesis conditions, showed that only with Eu a change in NPs shape occurs. Fig. 4a reports the SAED picture obtained with a particle of Eu:Hem_2, the corresponding micrograph and simulated patterns being in Fig. 4b and c, respectively. Overlapping of SAED data and morphology micrograph shows that the principal axes of rice grain-like particles are oriented along definite directions, i.e. the major and the minor axis correspond to the [1 View the MathML source1‾ 0] and [1 1 0] directions, respectively (Fig. 4a). This shows that the co-precipitation of Eu3+ and Fe3+ ions favours the crystal growth along the [1 View the MathML source1‾ 0] direction, hindering that along the [0 0 1] direction.
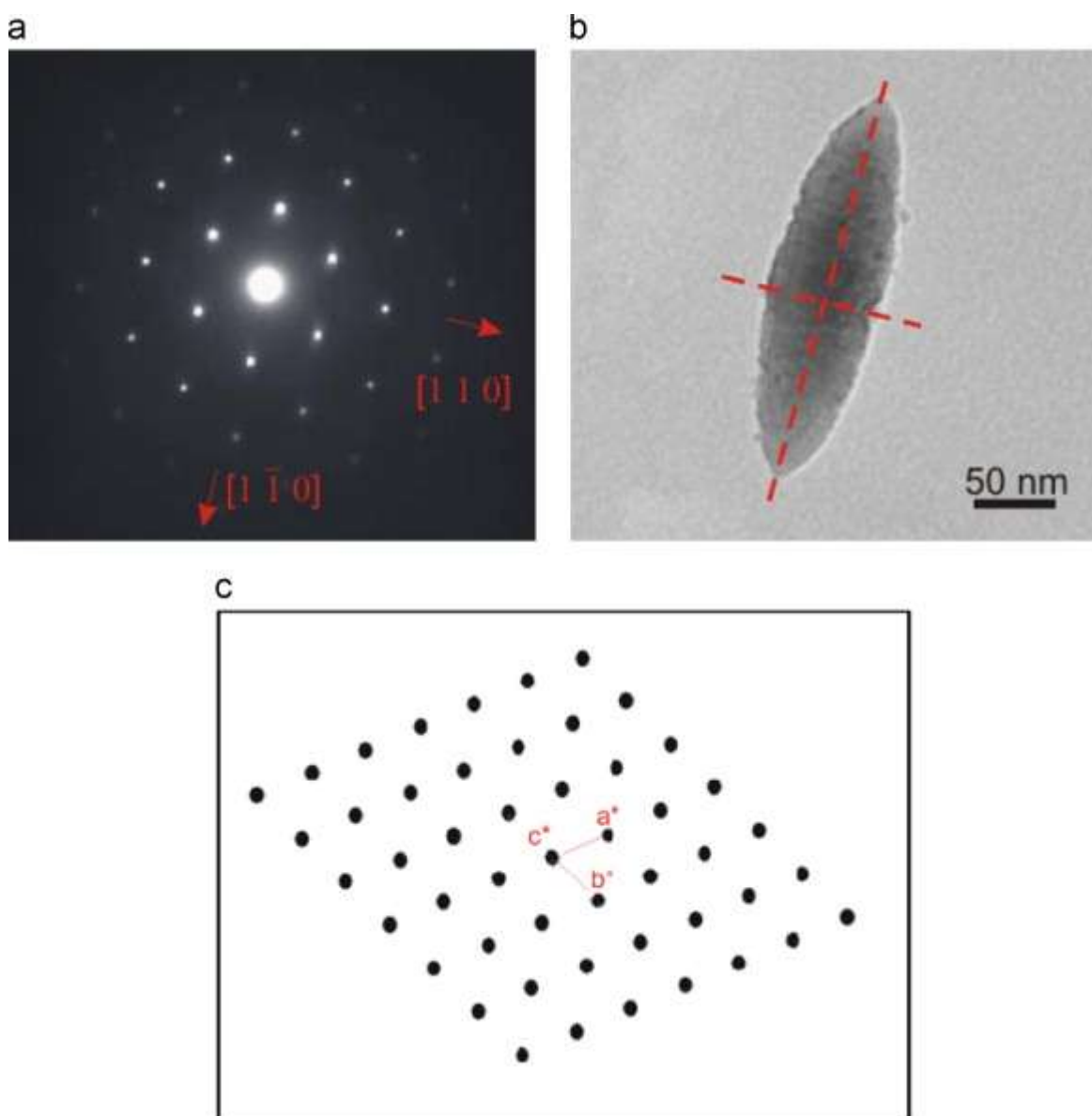
Fig. 4.

Sample Eu:Hem_2: (0 0 1) SAED pattern (a); corresponding morphological TEM micrograph (b) and simulated (0 0 1) electron pattern (c).

TEM micrographs (Fig. 3d and Fig. 4b) show a darker (i.e. denser) core in several rice grain-like particles, so suggesting that the more radiation-absorbing Eu cations are more abundant at NPs core. This seems to suggest that during nucleation, Fe^{3+} and Eu^{3+} cations compete for octahedral positions, with Eu^{3+} isomorphically substituting Fe^{3+}, then NPs grow in an environment progressively poorer in Eu.

3.2. Surface analysis by means of XP spectroscopy

Table 4 reports surface chemical composition as determined by XPS analysis: the surface atomic percentage of Eu increases, as expected, with the overall Eu content, but remains smaller than that in the bulk, as measured by both EDS analysis and Eu occupancy. This observation supports the idea that Eu content is larger at the core of NPs, as suggested by TEM pictures.

Table 4.

Surface composition (atomic percentage, at. %) as obtained from Eu 3d, O 1s and Fe 2p XPS lines, respectively.

Element	Sample		
	Hem	Eu:Hem_2	Eu:Hem_4
Eu (at%)	–	0.9	2.7
O (at%)	57.7	59.5	65.9
Fe (at%)	42.3	39.7	31.4

Fig. 5a reports high resolution O 1s XP spectra of the samples studied. Hem (curve a) shows two main components at 529.5 and 531.05 eV, assigned to surface O^{2-} and OH^- species, respectively [27]. With Eu:Hem_2 and Eu:Hem_4, the O^{2-} peak is seen at 529.21 and 529.27 eV, respectively, i.e. this peak is shifted towards lower BE values with respect to hematite alone. Since the O 1s BE for Eu_2O_3 is at 529.0 eV [28], the observed shift is in agreement with the presence of Eu cations bound to oxygen anions. A similar observation is probably valid for the OH^- peak at ca. 531 eV. O 1s spectra of Eu containing samples also show a component at ca. 533 eV, best seen in the spectral simulation in Fig. 5b, concerning Eu:Hem_2. This is assigned to water molecules [27], the presence of which is probably related to ferrihydrite: indeed, such component is more intense with Eu:Hem_4, featuring a larger content of ferrihydrite (vide supra) [28], [29] and [30].
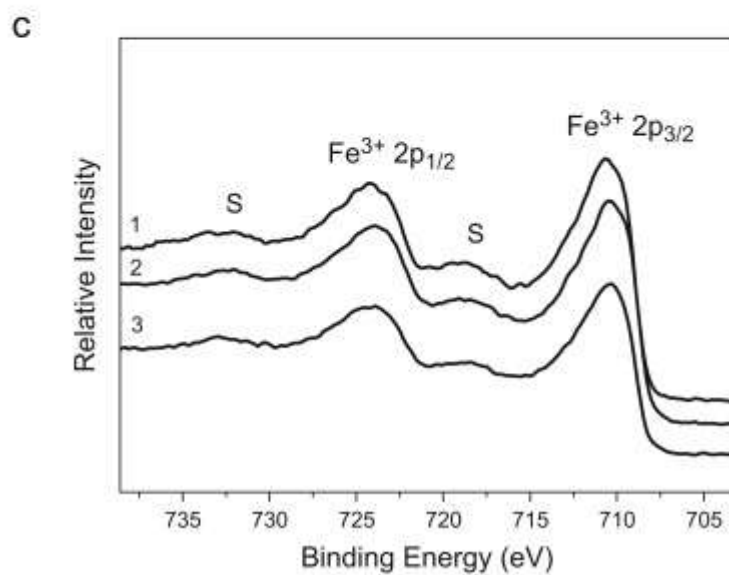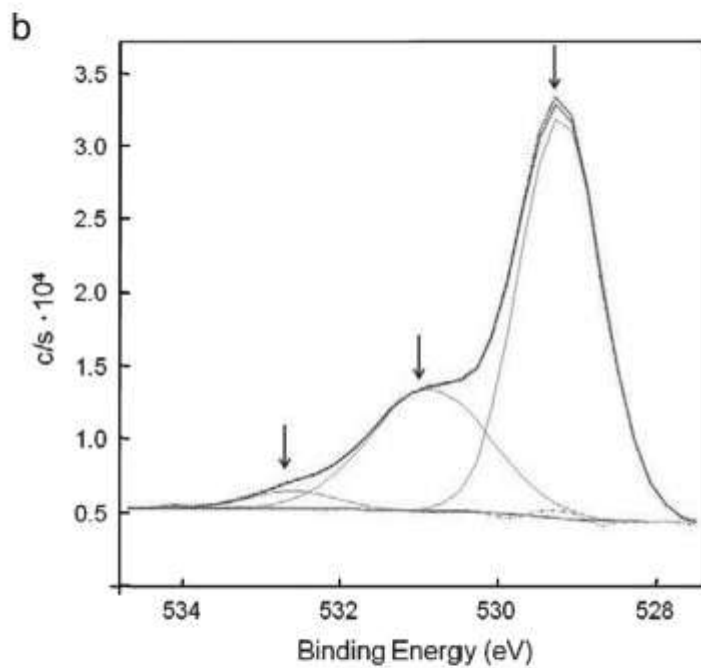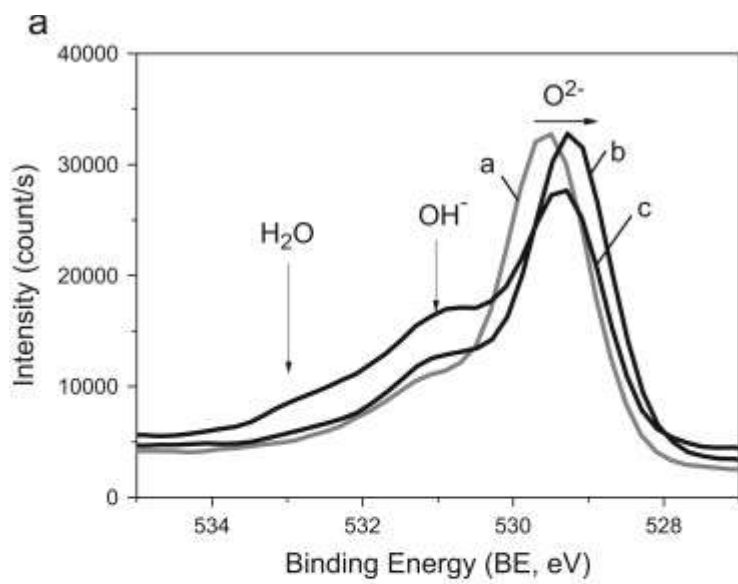
Fig. 5.

Section (a) O 1s XPS spectra of Hem; Eu:Hem_2 and Eu:Hem_4 (curves a, b, and c, respectively). Section (b) computer-resolution of the O 1s XPS spectrum of Eu:Hem_2 sample. Section c: Fe 2p XPS spectra of: Hem (1), Eu:Hem_2 (2), Eu:Hem_4 (3), S indicates satellite peaks.

Fig. 5c reports XPS spectra in the region where the Fe 2p lines occur: the three spectra show two peaks, at ca. 710.6 and 724.2 eV, attributed to trivalent Fe 2p3/2 and Fe 2p1/2, respectively, both having a satellite peak located approximately 8 eV higher than the main peak [33].

Whereas the interpretation of O and Fe lines is well established, that of Eu lines in XPS spectra is debated, and disagreements in the related literature are found [28] and [34]. For this reason, we restrict ourselves to an empiric use of these XPS data. Fig. 6a shows Eu 3d core-level XP spectra: with Eu:Hem_2 and Eu:Hem_4 (curves 1 and 2, respectively) a doublet is seen at 1134.27 and 1163.99 eV BE, corresponding to a spin–orbit splitting of 29.72 eV, whereas the lines of Eu 4d core-level XP spectra lie at 136.22 and 141.88 eV, with a spin–orbit splitting of 5.66 eV (Fig. 6b). Such results suggest that only trivalent Eu cations are present at the surface of both Eu:Hem_2 and Eu:Hem_4 samples. Eu Auger peaks and/or plasmonic peaks (labelled "A/P") were also detected (Fig. 6a) [31] and [32].
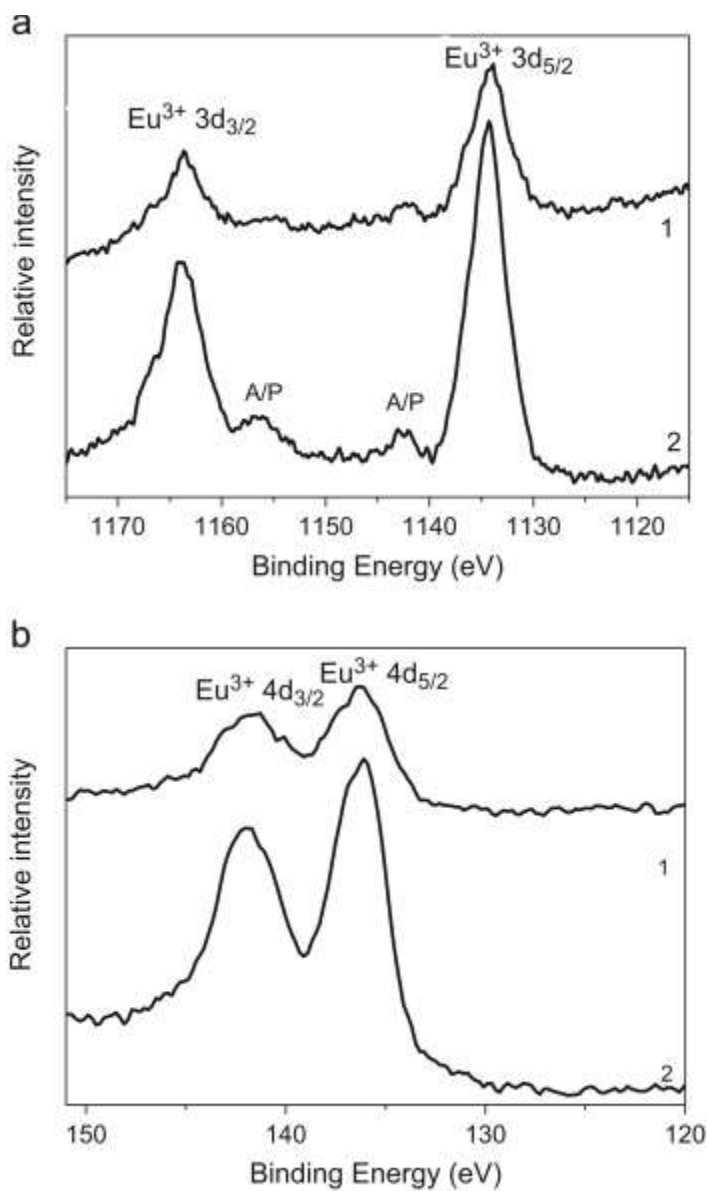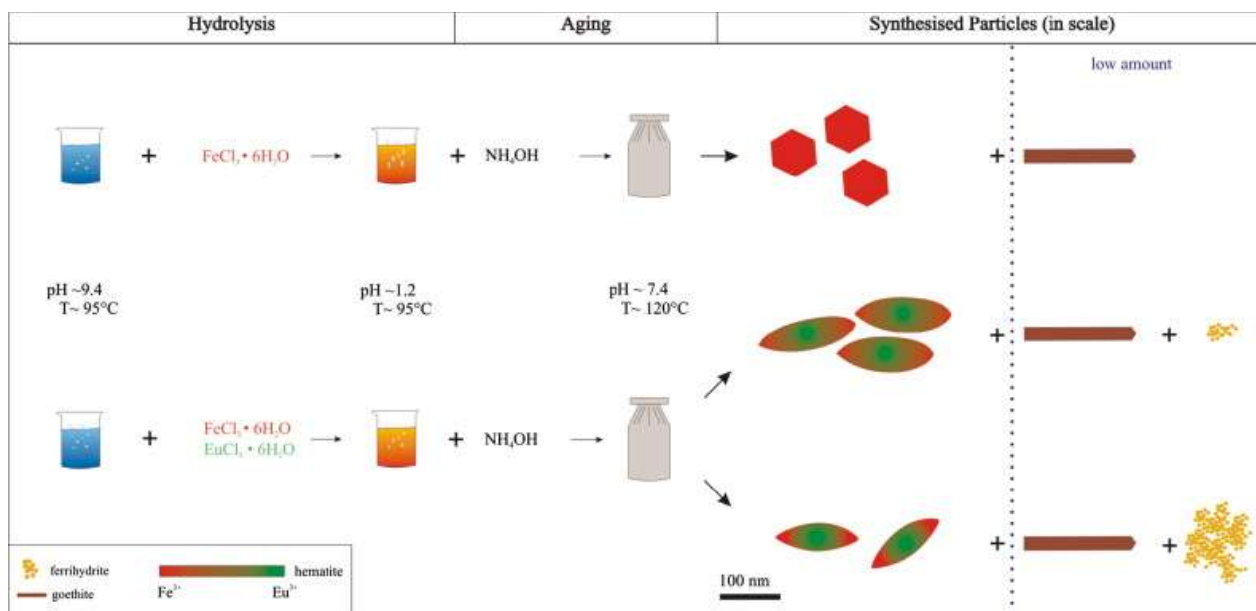
Fig. 6.

XPS spectra of, Eu:Hem_2 (1), Eu:Hem_4 (2) in the Eu 3d region (a) and Eu 4d region (b). A/P stands for Auger and/or plasmonic peaks (sections (a) and (b)).

3.3. Overall scheme for NPs formation

A mechanism of formation of Eu-doped hematite particles accounting for the evidence gained so far is shown in Scheme 1.

Scheme 1.

Synthesis process of Eu doped hematite particles. .

In water, ferric chloride dissolves forming hexa-aquo ions, which, under proper conditions, can be completely hydrolyzed to yield ferric oxides/hydroxides. In alkaline conditions, simple chemical species form initially, e.g. $Fe(OH)^{2+}$ or $Fe(OH)_4^-$, which then generate polynuclear/polymeric species by forming hydroxo (–Fe–OH–Fe) and oxo bonds (–Fe–O–Fe–). An increase of the OH/Fe ratio favours polymerisation to poorly ordered polynuclear species with respect to the precipitation of crystalline goethite (α-FeOOH). The products of hydrolysis and, consequently, the precursors needed for the crystals growth are influenced by the rate of hydrolysis, which can be increased by adding a base, heating or diluting the solution. Amorphous ferrihydrite firstly forms chains or rafts, which can transform into either goethite or hematite (Scheme 1). At pH around either 4 or 12, the formation of goethite is favoured, because it occurs through dissolution of ferrihydrite followed by nucleation. On the other hand, hematite forms via ferrihydrite aggregates by dehydration and rearrangement processes. At pH 7–8, the rate of ferrihydrite dissolution is very low, therefore the formation of hematite is favoured with respect to goethite. The final size of hematite particles depends on the dimension of ferrihydrite aggregates. The free energies of formation of goethite and hematite from 2-line ferrihydrite are quite similar and the predominance of one or the other is mainly controlled by the kinetics of reaction. Therefore, in a forced hydrolysis, the formation of ferrihydrite aggregates and the consequent transformation into hematite particles is faster, the precipitation increases while the rate of dissolution falls, preventing goethite formation. Foreign cations can influence particles formation and growth by a structural incorporation, which usually either hinder the crystal growth or retard the ferrihydrite dissolution.

In order to obtain Eu incorporation, aging at high temperature (393 K) and an alkaline environment are needed, conditions at which europium ions may compete with ferric cations by forming particles with a core probably richer in Eu than the surface (Fig. 4b).

3.4. Magnetic analysis

Pure hematite exhibits a spin-flip transition at the Morin temperature TM [35]; below TM, hematite is an antiferromagnetic (AF) compound with Fe^{3+} spins oriented along the c-axis of the hexagonal corundum cell; above TM it becomes a canted anti-ferromagnet with Fe^{3+} spins now lying in the basal plane of the cell; the Morin temperature marks therefore the onset of weak (parasitic) ferromagnetism resulting from incomplete balance of canted spins. Another ferromagnetic signal arising from defects (hence termed defect ferromagnetism) can be usually observed both below and above TM [36]. The Morin transition of the examined materials was studied by measuring the remanent magnetization on cooling all samples from 320 K down to 100 K, using the same procedure in order to avoid thermal hysteresis effects [37]. The measured data are reported in Fig. 7. The Morin transition is observed in all samples; the value of 226 K of undoped hematite is in good agreement with values reported in the literature for nanoparticles of similar size [35] and [37].
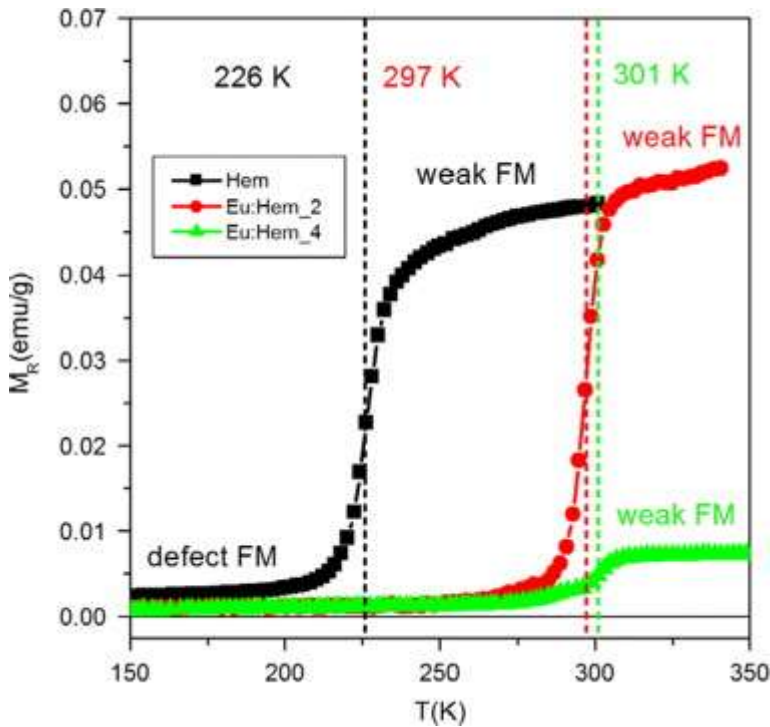

Fig. 7.

Remanent magnetization as a function of temperature in the 150–350 K range (curves taken on cooling, with the same cooling rate). Regions characterized by a different ferromagnetic (FM) behavior are indicated.

TM shifts towards higher temperatures by adding Eu cations, quite independently of the dopant concentration (values reported in Fig. 7 correspond to the maximum of the derivative of the MR vs. T curves). Isothermal magnetization loops were performed in the same temperature interval. Selected results are shown in Fig. 8; these curves are representative of the magnetic behaviour of all samples in the entire range of temperatures below and above TM, respectively. Below TM all samples are characterized by a M(H) response close to a straight line, as expected from ideal AF materials (such as nanopowders) whose magnetic susceptibility is constant and isotropic; above TM all samples exhibit a variety of novel features superimposed to the AF straight line (whose slope changes too). The total signal is viewed as the sum of two contributions, one arising from the AF phase and the other one from a ferromagnetic phase related to defects; as customary in these cases, the ferromagnetic behaviour is singled out by determining the AF contribution from a fit of each experimental curve to a straight line at sufficiently high fields (typically, $|H|>1\times10^4$ Oe), and by subtracting this line from the data of Fig. 8; the results are shown in Fig. 9. In summary:

a)

   defect ferromagnetism exists in all samples, as attested by the ferromagnetic signal detected below TM, which is particularly enhanced in Eu:Hem_4

b)

   the ferromagnetic signal above TM is associated to the onset of weak ferromagnetism; the new regime is most evident in undoped hematite and Eu:Hem_2, although with different shapes of the ferromagnetic loop; sample Eu:Hem_4 displays a modest increase in the ferromagnetic signal on top of an already significant contribution from defect ferromagnetism.
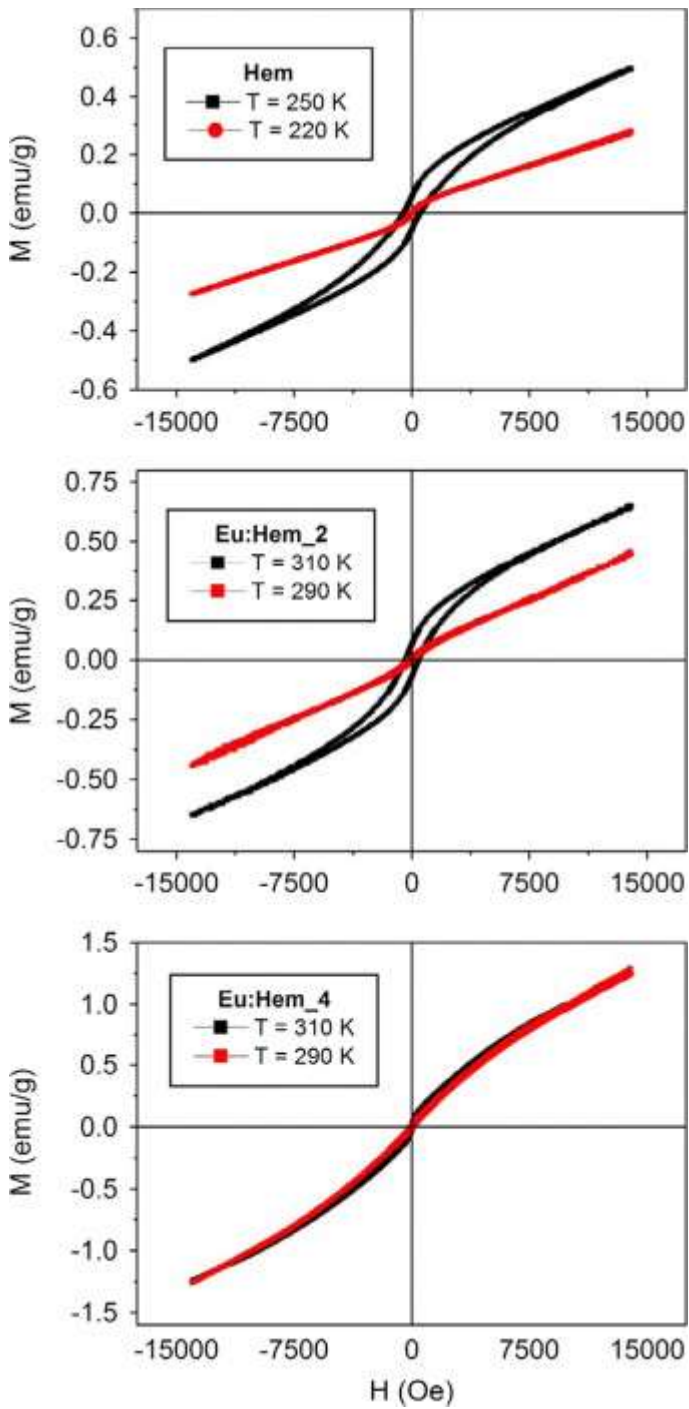
Fig. 8.

Isothermal magnetization loops taken at temperatures above (black curve) and below (red curve) TM for all studied samples; top panel: Hem; middle panel: Eu:Hem_2; bottom panel: Eu:Hem_4. (For interpretation of the references to color in this figure legend, the reader is referred to the web version of this article.)

Fig. 9.

The same as in Fig. 8 after subtraction of the linear response from the antiferromagnetic phase. Different ferromagnetic order states (FM) are indicated.

The role of Eu doping of the magnetic response of hematite nanoparticles can be put in evidence starting from the following considerations:

a)

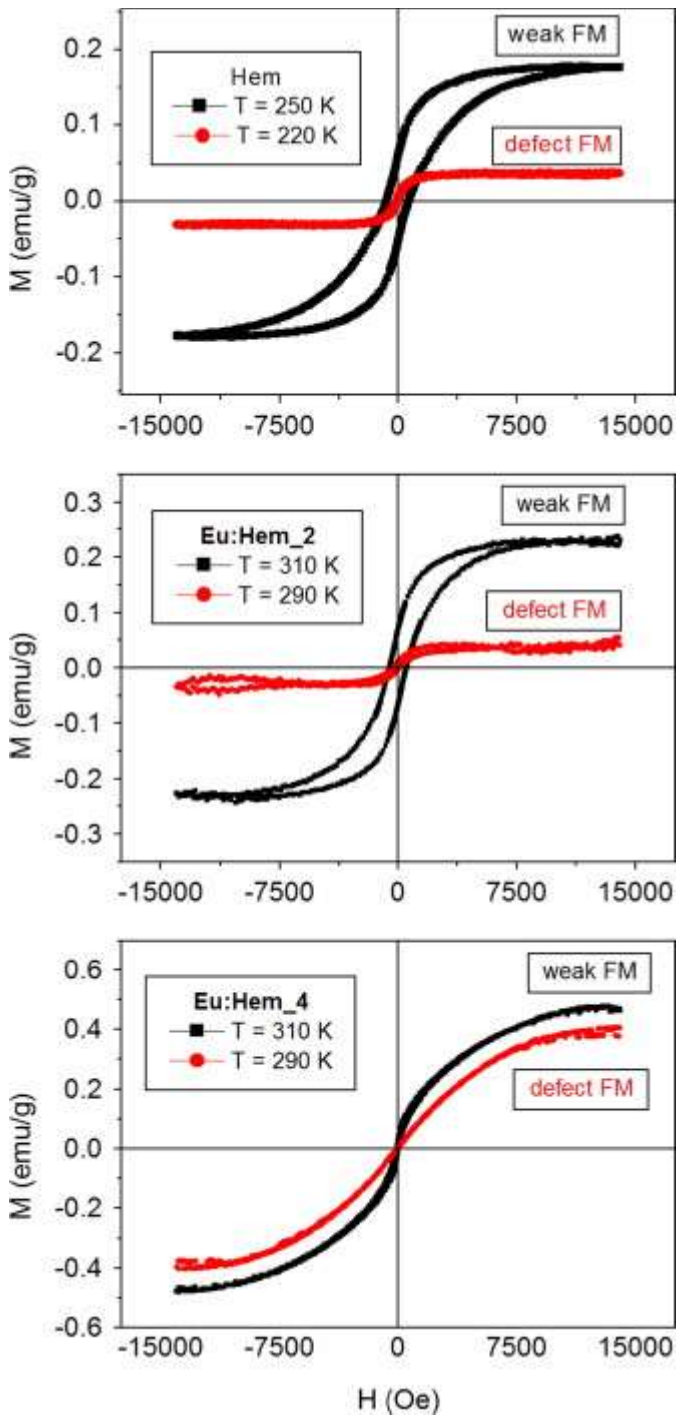trivalent Eu ions have an effective magnetic moment $\mu_{eff} \cong 3.3–3.5$ μB around room temperature [38]; this is markedly smaller than that of Fe^{3+} ions ($\mu_{eff}=5.9$ μB);

b)

rare-earth ions are characterized by a strong single-ion magnetic anisotropy arising from spin–orbit coupling [39] and higher than the one exhibited by transition metal ions.

The Morin transition involves flipping of magnetic moments away from the c-axis to the basal plane of the corundum cell. Spin flip arises by effect of the interplay of two competing magnetic anisotropy terms, one of single-ion nature and favouring the alignment of moments along the c-axis, the other of dipolar nature and favouring the alignment on the basal plane [40]. Below T_M the first term prevails; above T_M the second one becomes predominant. Addition of dopant ions characterized by a strong single-ion anisotropy favours a displacement of T_M towards higher temperatures, as observed (see Fig. 7). Such a shift is even more remarkable if one considers that the usually the Morin transition temperature in hematite nanoparticles and/or nanostructures sharply drops with decreasing size in the 10–100 nm range [37] and [41]. Using the data from Table 1 and assuming that rice-like NPs can be approximated as ellipsoids of revolution, the volumes of our samples range from $V \cong 1.6 \times 10^{-16}$ cm3 for Eu:Hem_4 to $V \cong 2.2 \times 10^{-16}$ cm3 in pure hematite to $V \cong 2.8 \times 10^{-16}$ cm3 in sample Eu:Hem_2. Therefore, the shift of T_M observed in Eu:Hem_4 with respect to pure hematite NPs can be safely ascribed to the effect of Eu cations, which dominates over the opposite effect of size; instead, in Eu:Hem_2 both Eu doping and an increase in volume concur to the observed displacement; this may explain why the overall shift is almost the same in the two doped samples, quite independently of Eu concentration; however, more compositions would be needed to support this conclusion.

On the other hand, trivalent Eu ions randomly substituting for Fe^{3+} ions in the crystal act as magnetic defects (their magnetic moment being smaller than the one required to get the perfect AF phase); as a consequence, defect ferromagnetism must increase (both below and above T_M) with increasing Eu^{3+} concentration, as indeed observed in Eu:Hem_4. Apparently, the presence of Eu^{3+} ions above some threshold acts to weaken the antiferromagnetic order not only below the Morin transition temperature but also above it, as shown by the very small weak ferromagnetism observed in Eu:Hem_4 (Fig. 7). Weak ferromagnetism above T_M arises out of the spontaneous spin-canting effect whose occurrence and magnitude are expected to critically depend on the degree of alignment of the ferromagnetic phase below T_M. An imperfect alignment originating from a number of defects may bring about a less pronounced canting of spins, resulting in a smaller uncompensated moment and a reduced effect of weak ferromagnetism. In fact, in sample Eu:Hem_4 the difference in both magnitude and shape between subtracted magnetization curves below and above T_M is very small (Fig. 9), suggesting that defect magnetism plays the fundamental role at all temperatures in this sample. Further measurements are however needed to clarify this point.

4. Conclusions

The synthesis conditions, particularly temperature and pH, have a marked effect on Eu-doping. High-temperature hydrolysis in basic conditions allows the obtainment of NPs with controlled dimension and morphology, together with other unwanted iron oxide/hydroxides, present, however, in minor amounts. The presence of Eu has a macroscopic effect on NPs shape, changing from cubic (pure hematite NPs) to rice grain-like (Eu-doped NPs). At the atomic scale, lattice parameters vary linearly with Eu content, with Eu ions preferentially substituting Fe ions along the [11$\bar{1}$0] axis, as observed in SAED measurements. Eu is found especially at NPs core, which results enriched with respect to the surface. This is ascribed to a mechanism consisting in nucleation as a first step, followed by growth during aging in autoclave, when the synthesis medium is poorer in Eu.

As to magnetic properties, addition of Eu cations causes the Morin temperature to move towards higher values; defect ferromagnetism above and below TM is enhanced. The results are interpreted by considering that trivalent Eu cations are characterized by higher one-ion anisotropy and lower magnetic moment with respect to Fe cations of the host structure.

References

[1]

T. Sugimoto, A. Muramatsu, K. Sakata, D. Shindo

J. Colloid Interface Sci., 158 (1993), pp. 420–428

[2]

L. Wang, L. Gao

J. Am. Ceram. Soc., 91 (2008), pp. 3391–3395

[3]

M. Mohapatra, D. Behera, S. Layek, S. Anand, H.C. Verma, B.K. Mishra

Cryst. Growth Des., 12 (2012), pp. 18–28

[4]

Q.A. Pankhurst, J. Connolly, S.K. Jones, J. Dobson

J. Phys. D: Appl. Phys., 36 (2003), p. R167

[5]

A.S. Teja, P.-Y. Koh

Prog. Cryst. Growth Charact. Mater., 55 (2009), pp. 22–45

[6]

Y.-B. Hahn, R. Ahmad, N. Tripathy

Chem. Commun., 48 (2012), pp. 10369–10385

[7]

R.M. Cornell, U. Schwertmann

The Iron Oxides: Structure, Properties, Reactions, Occurrences and Uses

Wiley-VCH, New York (1996) 2nd, Completely Revised and Extended Edition

[8]

T.P. Raming, A.J.A. Winnubst, C.M. van Kats, A.P. Philipse

J. Colloid Interface Sci., 249 (2002), pp. 346–350

[9]

F.S. Freyria, B. Bonelli, M. Tomatis, M. Ghiazza, E. Gazzano, D. Ghigo, E. Garrone, B. Fubini

Chem. Res. Toxicol., 25 (2012), pp. 850–861

[10]

Y. Xu, S. Yang, G. Zhang, Y. Sun, D. Gao, Y. Sun

Mater. Lett., 65 (2011), pp. 1911–1914

[11]

T. Sugimoto, H. Itoh, T. Mochida

J. Colloid Interface Sci., 205 (1998), pp. 42–52

[12]

T. Nagano, H. Mitamura, S. Nakayama, S. Nakashima

Clays Clay Miner., 47 (1999), pp. 748–754

[13]

N.C. Pramanik, T.I. Bhuiyan, M. Nakanishi, T. Fujii, J. Takada, S.I. Seok

Mater. Lett., 59 (2005), pp. 3783–3787

 [14]

T.I. Bhuiyan, M. Nakanishi, Y. Kusano, T. Fujii, J. Takada, Y. Ikeda

Mater. Lett., 61 (2007), pp. 3774–3777

 [15]

Q. Liu, K. Osseo-Asare

J. Colloid Interface Sci., 231 (2000), pp. 401–403

 [16]

T. Sugimoto, Y. Wang, H. Itoh, A. Muramatsu

Colloids Surf., A, 134 (1998), pp. 265–279

 [17]

T. Sugimoto, Y. Wang

J. Colloid Interface Sci., 207 (1998), pp. 137–149

 [18]

T. Sugimoto, K. Sakata, A. Muramatsu

J. Colloid Interface Sci., 159 (1993), pp. 372–382

 [19]

K. Kandori, J. Sakai, T. Ishikawa

Phys. Chem. Chem. Phys., 2 (2000), pp. 3293–3299

 [20]

A.U. Pawar, A.P. Jadhav, U. Pal, B. Kyu Kim, Y.Soo Kang

J. Lumin., 3 (2011), pp. 659–664

[21]

A.C. Larson, R.B. Von Dreele

Gen. Struct. Anal. Syst. (GSAS) (2000), pp. 86–748

[22]

B. Toby

J. Appl. Crystallogr., 34 (2001), pp. 210–213

[23]

U. Schwertmann, E. Murad

Clays Clay Miner., 31 (1983), pp. 277–284

[24]

J. Zhao, F.E. Huggins, Z. Feng, G.P. Huffman

Clays Clay Miner., 42 (1994), pp. 737–746

[25]

Y. Cudennec, A. Lecerf

J. Solid State Chem., 179 (2006), pp. 716–722

[26]

R. Shannon

Acta Crystallogr., Sect. A: Cryst. Phys., Diffr., Theor. Gen. Crystallogr., 32 (1976), pp. 751–767

[27]

J.A. Mielczarski, G.M. Atenas, E. Mielczarski

Appl. Catal., B, 56 (2005), pp. 289–303

[28]

F. Mercier, C. Alliot, L. Bion, N. Thromat, P. Toulhoat

J. Electron Spectrosc. Relat. Phenom., 150 (2006), pp. 21–26

[29]

D.-Y. Lu, M. Sugano, X.-Y. Sun, W.-H. Su

Appl. Surf. Sci., 242 (2005), pp. 318–325

[30]

R. Abu-Much, A. Gedanken

J. Phys. Chem. C, 112 (2007), pp. 35–42

[31]

D.F. Mullica, C.K.C. Lok, H.O. Perkins, G.A. Benesh, V. Young

J. Electron Spectrosc. Relat. Phenom., 71 (1995), pp. 1–20

[32]

R. Vercaemst, D. Poelman, R.L. Van Meirhaeghe, L. Fiermans, W.H. Laflère, F. Cardon

J. Lumin., 63 (1995), pp. 19–30

[33]

T. Yamashita, P. Hayes

Appl. Surf. Sci., 254 (2008), pp. 2441–2449

[34]

W.-D. Schneider, C. Laubschat, I. Nowik, G. Kaindl

Phys. Rev. B: Condens. Matter Mater. Phys., 24 (1981), pp. 5422–5425

[35]

S. Chikazumi

Physics of Ferromagnetism

(1997 ed.)Oxford University Press, Oxford (1997)

[36]

Ö. Özdemir, D.J. Dunlop

J. Geophys. Res., 111 (2006), p. B12S03

[37]

Ö. Özdemir, D.J. Dunlop, T.S. Berquó

Geochem. Geophys. Geosyst., 9 (2008), p. Q10Z01

[38]

Y. Takikawa, S. Ebisu, S. Nagata

J. Phys. Chem. Solids, 71 (2010), pp. 1592–1598

[39]

R. Skomski

Simple Models Magn. (2008)

[40]

J.O. Artman, J.C. Murphy, S. Foner

Phys. Rev., 138 (1965), pp. A912–A917

[41]

C. Eid, D. Luneau, V. Salles, R. Asmar, Y. Monteil, A. Khoury, A. Brioude

J. Phys. Chem. C, 115 (2011), pp. 17643–17646